



Leading opinion

Textured and hierarchically structured calcium phosphate ceramic blocks through hydrothermal treatment



Laetitia Galea ^{a, b}, Dmitriy Alexeev ^c, Marc Bohner ^{a, *}, Nicola Doebelin ^a, André R. Studart ^c, Christos G. Aneziris ^b, Thomas Graule ^{b, d}

^a RMS Foundation, Bischmattstrasse 12, CH-2544 Bettlach, Switzerland

^b Technical University Bergakademie Freiberg, Institute for Ceramic, Glass- and Construction Materials, Agricolastraße 17, 09596 Freiberg, Germany

^c Complex Materials, Department of Materials, ETH Zürich, 8093 Zürich, Switzerland

^d EMPA, Swiss Federal Laboratories for Materials Science and Technology, Laboratory for High Performance Ceramics, Ueberlandstrasse 129, 8600 Dübendorf, Switzerland

ARTICLE INFO

Article history:

Received 22 April 2015

Received in revised form

10 July 2015

Accepted 13 July 2015

Available online 16 July 2015

Keywords:

Calcium phosphate

Hydrothermal treatment

Hierarchical structures

Strength

Toughness

Work-of-fracture

ABSTRACT

Synthetic calcium phosphate bone graft substitutes are widely recognized for their biocompatibility and resorption characteristics in the treatment of large bone defects. However, due to their inherent brittleness, applications in load-bearing situations always require reinforcement by additional metallic implants. Improved mechanical stability would eliminate the need for non-resorbable metallic implants. In this context a new approach to obtain calcium phosphate scaffolds with improved mechanical stability by texturing the material in specific crystal orientations was evaluated. Texture and reduction of crystal size was achieved by recrystallizing α -TCP blocks into calcium deficient hydroxyapatite (CDHA) under hydrothermal conditions. SEM and XRD analysis revealed the formation of fine CDHA needles (diameter \approx 0.1–0.5 μ m), aligned over several hundreds of micrometers. The obtained microstructures were remarkably similar to the microstructures of the prismatic layer of mollusk shells or enamel, also showing organization at 5 hierarchical structure levels. Brazilian disc tests were used to determine the diametral tensile strength, σ_{dts} , and the work-of-fracture, WOF, of the textured materials. Hydrothermal incubation significantly increased σ_{dts} and WOF of the ceramic blocks as compared to sintered blocks. These improvements were attributed to the fine and entangled crystal structure obtained after incubation, which reduces the size of strength-determining critical defects and also leads to tortuous crack propagation. Rupture surfaces revealed intergranular tortuous crack paths, which dissipate much more energy than transgranular cracks as observed in the sintered samples. Hence, the refined and textured microstructure achieved through the proposed processing route is an effective way to improve the strength and particularly the toughness of calcium phosphate-based ceramics.

© 2015 Elsevier Ltd. All rights reserved.

1. Introduction

Calcium phosphate (CaP) ceramics are widely used as bone graft substitute materials, the majority of commercial porous scaffolds being composed of β -tricalcium phosphate (β -TCP), hydroxyapatite (HA) or a blend of both phases (biphase). Many CaP ceramics combine high biocompatibility, adequate resorption rate and porosity for nutrient supply, vascularization, cell proliferation, and tissue infiltration [1,2]. While some phases are soluble at

physiological pH and dissolve spontaneously in-vivo, others are insoluble and can only be actively resorbed by bone cells [3]. However, ceramics CaP scaffolds are very brittle with a fracture toughness well below 1 MPa·m^{1/2}. In comparison, cortical bone has a true fracture toughness over 20 MPa·m^{1/2} [4]. These properties limit the use of CaP materials to indications in which the implant is not subjected to mechanical loading. Cyclic dynamic loading would lead to cracking and displacement of the surrounding bone fragments would delay or inhibit bone formation and thus impair successful healing of the defect. All CaP scaffolds commercially available can therefore only be applied in situations where either intact bone or additional metal implants protect the ceramic bone void filler from mechanical stress. The availability of novel load-

* Corresponding author.

E-mail address: marc.bohner@rms-foundation.ch (M. Bohner).

bearing resorbable scaffolds would eliminate the need for additional reinforcement and widen the scope of indications. Such a scaffold should be strong enough to support normal loading applied on the bone, its elastic modulus should be similar to the one of bone to avoid stress shielding, and high toughness would be necessary to prevent catastrophic failure.

Combination of high strength and toughness is rare in engineered materials because these properties are antagonistic [5]; single-phase materials are normally either strong and brittle, or ductile and weak. Obtaining a combination with biodegradable materials is even more challenging because biodegradability generally implies weak chemical bonds, which are in consequence rarely mechanically strong. Moreover, biocompatibility and biodegradability strongly limit the choice of materials. Ceramics are strong, but highly brittle. Metals can be adequate in terms of toughness, but they lead to stress shielding and are, with the exception of a few alloys [6–8], non-degradable. Generally, polymers do not reach the required strength and their degradation products can be acidic and/or provoke an inflammatory response, both adversely affecting the healing process [9].

Since no single-phase material seems to fulfill all requirements imposed by a load-bearing, resorbable bone graft substitute, the focus of researchers has shifted towards composite materials, which combine properties of materials of different nature. Reinforcement of degradable polymers by ceramic particles has already been extensively investigated [10–15]. However, in all of these studies, the organic fraction remained large which might cause the above-mentioned biological complications [9]. In addition, mechanical properties of such artificial composites are by far inferior to comparable natural materials [16], which is mainly attributed to a poor adhesion between organic and inorganic phases [17] and a lack of controlled architecture of the reinforcing particles within the matrix. To achieve the ideal mechanical and biological properties for a load-bearing, resorbable bone graft substitute, the materials should mainly consist of ceramic, should be toughened with only minor amounts of a ductile polymer and the ceramic-polymer adhesion should be good. To approach this ideal material incorporating only thin interlayers of a tough secondary phase [18], bio-inspired structures featuring a highly organized architecture of the ceramic particles are necessary. A low polymer content and a large contact area between polymer and ceramic particles can only be obtained with a very well organized architecture. In fact, mechanical properties approaching those of natural composites like bone or nacre have been achieved with very well-controlled alignment of ceramic particles [4,19,20]. However, despite the highly ordered particle shape and arrangement, the polymer fraction was still much higher than the content found in nacre or even bone, and the ceramic particles were not degradable.

Toughening ceramic based materials by incorporating low fraction of polymer phases (“intrinsic toughening” [18,21]) remains a very challenging approach with current engineering methods and the reported improvements are limited. Considering the difficulty to achieve intrinsic toughening where a ceramic is arranged in a very well ordered manner and glued together by the polymer, a first approach might be to try to produce highly ordered polymer-free architectures, where the toughness is mainly improved due to structural changes (defined as “extrinsic toughening” mechanisms in Refs. [21,18]).

Indeed, strength and toughness of structural ceramics are usually improved by microstructural developments like (a) grain size refinement [22] – which already proved being efficient in bioceramics, in particular in HA [23], (b) transformation-toughening [24–27], (c) incorporation of second phase particles [28,29] or (d) creation of tortuous structures [18,30]. Tortuous structures are constituted of anisotropic particles, assembled in a staggered

fashion to promote crack deflection. Its good potential was demonstrated by the recently obtained “Nacre-like Alumina” [30]. However, to the best of our knowledge, this has not been investigated yet with bioceramics. A combination of grain size refinement and design of tortuous microstructures is a promising strategy to increase the work-of-fracture (WOF) of resorbable CaP ceramics by simultaneously decreasing the size of critical defects and inducing crack deflection.

CaP ceramic scaffolds are commonly shaped by pressing of a dry powder or drying/setting of a slurry, followed by a heat treatment (sintering) to consolidate the structure. With such methods, the final grain size strongly depends on the particle size of the initial powder, hence requiring nano-powders followed by quick sintering or two-step sintering processes in order to obtain a small final grain size [31]. Hydrothermal synthesis has already shown the potential of forming fine CaP (particularly HA) particles [32–34]. However, assembly and consolidation of these particles to form fine structured blocks, either by cement reaction or sintering, leads to grain growth and finally poor improvements of mechanical properties compared to larger microstructures [23,35,36]. Another approach, explored in particular by Ioku's group, consist in first compacting an α -TCP powder, with or without other additives, followed by submitting the pressed forms to hydrothermal treatment [37,38]. The obtained CDHA blocks were made of entangled rod-shape particles and were even more biodegradable and induced more bone formation than stoichiometric HA samples obtained by conventional sintering process [39]. However, the rod-shape crystal assembly was quite loose and disordered.

To densify and align the structures obtained in previous hydrothermal studies, our approach in this work was to first solidify and densify CaP blocks by sintering, and then globally refine the microstructure of these monoliths by *in situ* recrystallization under hydrothermal conditions. By obtaining a dense assembly of sub-micrometric elongated particles in complex architectures, we aimed at improving the strength and toughness of CaP scaffolds using a straightforward processing route.

2. Materials and methods

2.1. Sample preparation

CaP blocks were prepared in a process of 5 steps:

- (i) **Powder synthesis:** α -TCP powder was prepared in-house by ball-milling for 6 h at 60 rpm a sintered (4 h at 1350 °C, followed by air quenching) mixture of calcium carbonate (CaCO₃, art. no 102066, Merck, Darmstadt, Germany) and calcium hydrogen phosphate (CaHPO₄, 99.95%, art. no 1548, GFS Chemicals, Columbus OH, USA) such as to obtain an initial calcium to phosphate molar ratio of 1.47.
- (ii) **Cement paste preparation:** The liquid phase was a 0.1 M citric acid solution (C₆H₈O₇·H₂O, art. no 100243, Merck, Darmstadt, Germany). The powder was added to the liquid in a 0.6:1 liquid: powder weight ratio and immediately mixed (stirrer VOS 14, art. no. 441-0026P, VWR, Dublin, Ireland) at 2000 RPM for 20 s and then poured into cylindrical Teflon molds (8 mm diameter, 8 mm height).
- (iii) **Setting:** Setting took place in 100% RH at 60 °C for 72 h.
- (iv) **Sintering:** After unmolding, the samples were sintered at 1500 °C for 8 h with a heating rate of 5 °C/min and cooling at –10 °C/min in a muffle furnace (LHT 02/16, Nabertherm, Germany).
- (v) **Hydrothermal incubation:** Hydrothermal incubation was conducted in steel autoclaves (Acid Digestion Vessel, model 4744, Parr Instruments, Moline IL, USA) with homemade

inner Teflon capsules (inner volume of 45 ml), placed for 2–72 h at 125/150/175/200 °C. The samples were placed above the water level (7 ml) on perforated Teflon plates (Supplementary data, Figure S1). At the end of the incubation time, the autoclaves were cooled down for a few minutes in air, then in a water bath. The samples were finally dried for 24 h at 60 °C.

During the hydrothermal treatments, the water evaporation created a pressure increase equal to the saturated vapor pressure P . This increase is almost exponential with the temperature T :

$$\log_{10}(P) = A - \frac{B}{C+T} \quad (1)$$

with $A = 8.14019$, $B = 1810.94$ and $C = 244.485$ for $99\text{ °C} < T < 374\text{ °C}$ [40]. Hence, the pressure was 231, 473, 887 and 1552 kPa at 125, 150, 175 and 200 °C, respectively.

2.2. Sample characterization

After sintering and hydrothermal incubation, all samples were weighed and their external dimensions were measured with a caliper. Porosity was calculated taking into account the theoretical density of the phase composition obtained from the XRD analysis.

From each batch, at least one sample was ground and used for X-ray diffraction (XRD) analysis. Powder datasets were collected on a PANalytical CubiX diffractometer (PANalytical, Almelo, The Netherlands) using graphite-monochromated $\text{CuK}\alpha$ radiation. A range from 4 to $60^\circ 2\theta$ was scanned with a step size of $0.02^\circ 2\theta$ and a counting time of 1 s per step. The divergence slit was used in automatic mode set to an irradiated length of 10 mm. The datasets were analyzed by Rietveld refinement using the software BGMN version 4.2.22 [41] and structure templates from Schroeder et al. [42] for β -TCP, Mathew et al. [43] for α -TCP, Sudarsanan [44] for HA (or CDHA) and Dickens et al. [45] for DCP. The following parameters were refined: scale factor, unit cell parameters, anisotropic peak broadening, isotropic micro-strain, and preferred orientation.

The microstructure of the samples was investigated by Scanning Electron Microscope (SEM) (LEO 1530, Carl-Zeiss SMT AG, Oberkochen, Germany). All samples except polished ones for back-scattered electron (BSE) analysis were sputtered with platinum for 60 s at 40 mA and $5 \cdot 10^{-7}$ mbar in a sputter coater (BAL-TEC, SCD 050) before investigation. Samples for BSE analysis were coated with 2 carbon layers using the same device.

To determine the grain size after sintering, the samples were polished using 1000 then 2400 and finally P4000 grit Silicon Carbide abrasive paper (Reflex concept, Presi, Le Locle, Switzerland) on a polishing machine (Knuth-Rotor 2, Struers) using isopropanol as lubricant. The samples were then rinsed and thermally etched at 1300 °C for 20 min. The grain size was then measured on SEM images. Hydrothermally treated samples could not be thermally etched. Those samples were embedded, polished and chemically etched with 0.1 M HCl for 10 s at room temperature.

Crystal texturing (smaller crystals, oriented crystal domains) is known to positively affect the mechanical properties of ceramics. To get a preliminary assessment of the change of mechanical properties, small cylinders were submitted to diametral tensile strength measurements [46]. The transverse pressure load was applied with a Zwick (zwicki-Line Z5.0, Zwick, Kennesaw, GA, USA) at a constant displacement speed of 10 mm/min. The toughness could be estimated semi-quantitatively from the work of fracture, which was sufficient to track relative differences among the samples. The results were compared by ANOVA with a significance limit set at $p < 0.01$.

3. Results

3.1. Macroscopic observations and measurements

After the hydrothermal treatments and subsequent drying, the blocks could be manipulated without losing their integrity. Their weight and size were measured to verify their macroscopic shape and dimensions. No significant differences of diameter and height occurred during incubation, independently of the incubation conditions (time and temperature), but the porosity slightly but significantly increased from $31 \pm 2\%$ after sintering to $35 \pm 3\%$ after hydrothermal treatment (Supplementary data, Figure S2).

3.2. Microstructural changes (SEM)

One sample per composition/condition was broken by bending and the rupture surfaces were prepared for observation by SEM. Morphology changes were observed at the microscale. Recrystallization from the smooth sintered porous α -TCP structure (Fig. 1a) into fine elongated faceted structures occurred first around cracks and pores (Fig. 1b, enlarged in Fig. 1e). The conversion into faceted structures then progressed into the bulk of the α -TCP initial scaffold (Fig. 1c) with a rate strongly dependent on the temperature. At the end of the reaction, the whole sample was filled with needle-like crystals (Fig. 1d). The first crystals around cracks seemed rather disoriented (Fig. 1e), but large zones (from a few to hundreds of micrometers) with aligned crystals were later observed (Fig. 1d and f). Semi-quantitatively, conversion of about 0.5 μm from a surface (pore or crack) was measured after 2 h incubation at 125 °C and progressed up to about 3 μm after 8 h. At 150 °C, the converted thickness was similar at 2 h ($\approx 0.5\ \mu\text{m}$), but progressed already to about 5 μm after 4 h. At 175 °C, the converted thickness could only be measured after 2 h (about 5 μm) but not at later time points because it became too thick for SEM observation. At longer incubation times, the phase conversion appeared to be complete. Large crystals were also observed at the end of the reactions, especially at the highest temperatures and on the pore surfaces (Fig. 1f).

Differences in the location of needles were observed as a function of incubation temperature. At 125 °C, the needles completely invaded the microporosity (Fig. 2a; here, a micropore is considered to have a size in the range of 100 nm to 100 μm , but they protruded less into the initial porosity with increasing temperature (Fig. 2b). As a consequence, at low temperature the previously dense solid parts appeared more porous and also made of entangled needles (Fig. 2c). With increasing temperature, the needles were increasingly confined to the initial solid location, leading to much compacter structures and better alignment (Fig. 2c–f).

At low temperature, needles that grew into pores were longer and thicker than those growing in the solid phase and the opposite was observed at the highest temperature (Fig. 3). In the pores, the average diameter of the needles was not influenced by temperature (Fig. 3a), but their length was: the crystals were 10 times longer at 125 °C than at 200 °C (ANOVA: $p < 0.01$) (Fig. 3c). In the solid phase, both length (Fig. 3b) and diameter (Fig. 3d) of the needles increased with increasing incubation temperature ($p < 0.01$).

Determining quantitatively the size of the oriented domains proved to be very difficult. By etching polymer-impregnated and polished surfaces, it was possible to see that domains extending over hundreds of micrometers were also surrounded by some smaller ones (Fig. 4). For comparison, after sintering for 8 h at 1500 °C, the average grain size was about 30–100 μm .

3.3. Crystalline phase conversion (XRD)

The crystalline phase conversion was characterized by Rietveld

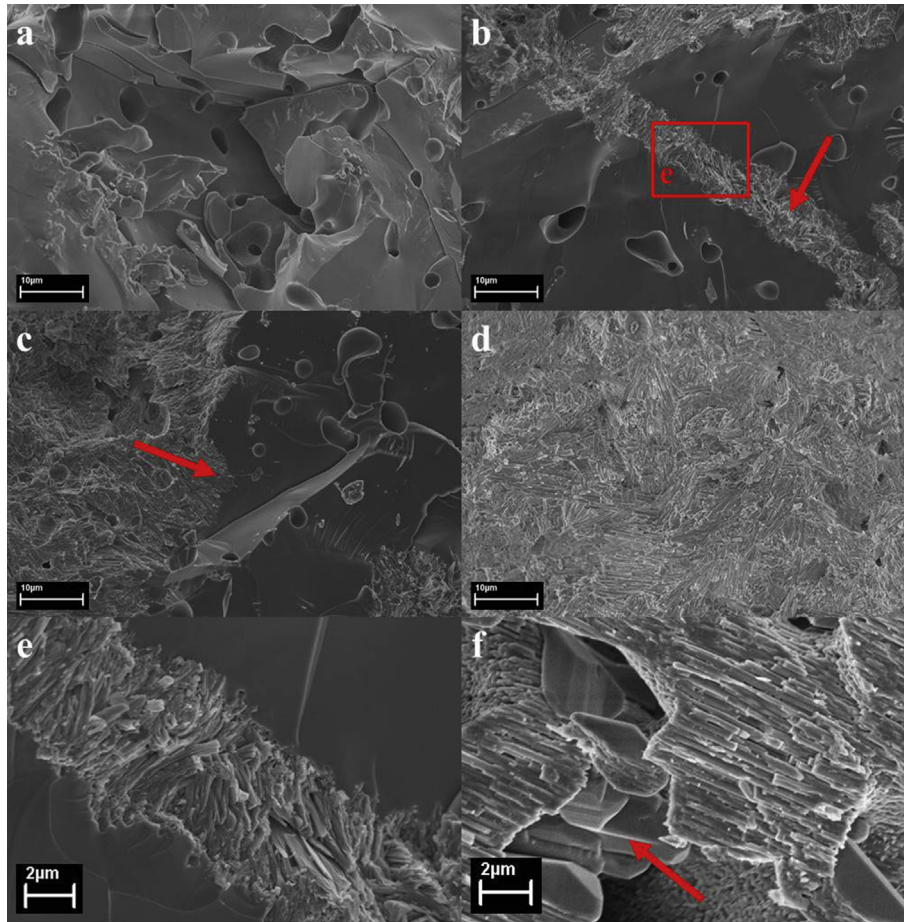


Fig. 1. Effect of incubation time on the microstructure as observed by SEM of broken surfaces. a) sintered α -TCP; b) incubation for 2 h at 175 °C: recrystallization into elongated hydroxyapatite crystals starts around cracks (arrow) and pores; c) incubation for 4 h at 175 °C: further growth of the needle-like structure into the bulk in one direction (arrow); d) incubation for 8 h at 175 °C: complete recrystallization; e) enlargement of b) on the newly formed crystals around a crack; f) large crystals (arrow) observed particularly in pores at the end of the reactions, especially a high temperature (here after 72 h of incubation at 200 °C). Scale bars are 10 μm in a to d and 2 μm in e and f.

refinement of XRD data. Various phases were detected during the hydrothermal incubation even though the initial 100% α -TCP blocks mainly converted into calcium deficient hydroxyapatite (CDHA) (Fig. 5a and b). β -TCP and monetite (DCP) phases were formed in amounts depending on the incubation temperature (Fig. 5c and d).

The conversion rate from α -TCP to CDHA and DCP increased with the incubation temperature (Fig. 5a and b). Increasing the temperature also accelerated and increased the formation of β -TCP (Fig. 5c), but β -TCP disappeared over time apparently in favor of CDHA and DCP. α -TCP almost completely disappeared but the contents of CDHA and DCP continuously increased until they reached a plateau. Hence, up to 10 wt-% of DCP were detected at the end of the reactions. The global Ca/P molar ratio of the samples was checked by XRD analysis after calcination at 900 °C for 24 h [47]. The resulting composition was a mixture of β -TCP (Ca/P = 1.5), β -CPP (Ca/P = 1.0) and HA (Ca/P = 1.667), corresponding to a global Ca/P molar ratio in the samples of 1.50.

Comparing XRD results and SEM observations, the needle-like crystals were identified as hydroxyapatite and the large prismatic ones (Fig. 1f) were attributed to the DCP phase. No structural features could be identified as β -TCP.

Evolution with time of all phase contents, $Y_i(t)$, were fitted with the Avrami equation [48]:

$$Y_i(t) = 1 - \exp(-K_i \cdot t^{n_i}), \quad (2)$$

where K_i is a constant related to the formation of phase i at a

given temperature and n_i is an integer. In a first step, both K and n were fitted. In a second step, only K was optimized with n set to the closest integer value found previously. All phase evolutions, except DCP, were best fitted with $n = 1$. DCP was best fitted with $n = 3$.

The consumption and formation of all crystalline phases were fitted, and their respective regression coefficients (R^2) calculated (Table 1). Whereas most of the fits were acceptable ($R^2 > 0.80$), some were quite poor, in particular for the consumption of β -TCP at high temperatures ($R^2 < 0.65$). However, fitting the sum of α -TCP and β -TCP fractions and the sum of DCP and HA fractions led to excellent fits with regression coefficients mainly larger than 0.90 (Table 1 and Fig. 5e).

The activation energy of each phase conversion was retrieved from a plot of K_i as a function of $1/T$ using Arrhenius equation (Table 1). The values were close to 25 kJ/mol for α -TCP consumption and HA formation, and were higher for β -TCP consumption (40 ± 6 kJ/mol) and DCP formation (119 ± 37 kJ/mol). In consequence, the activation energy for the combined CDHA and DCP formation or the combined α -TCP and β -TCP consumption was 30 ± 5 kJ/mol.

3.4. Mechanical properties

The fracture energy was calculated as the integral of the force-displacement curves until sample failure occurred (maximum force).

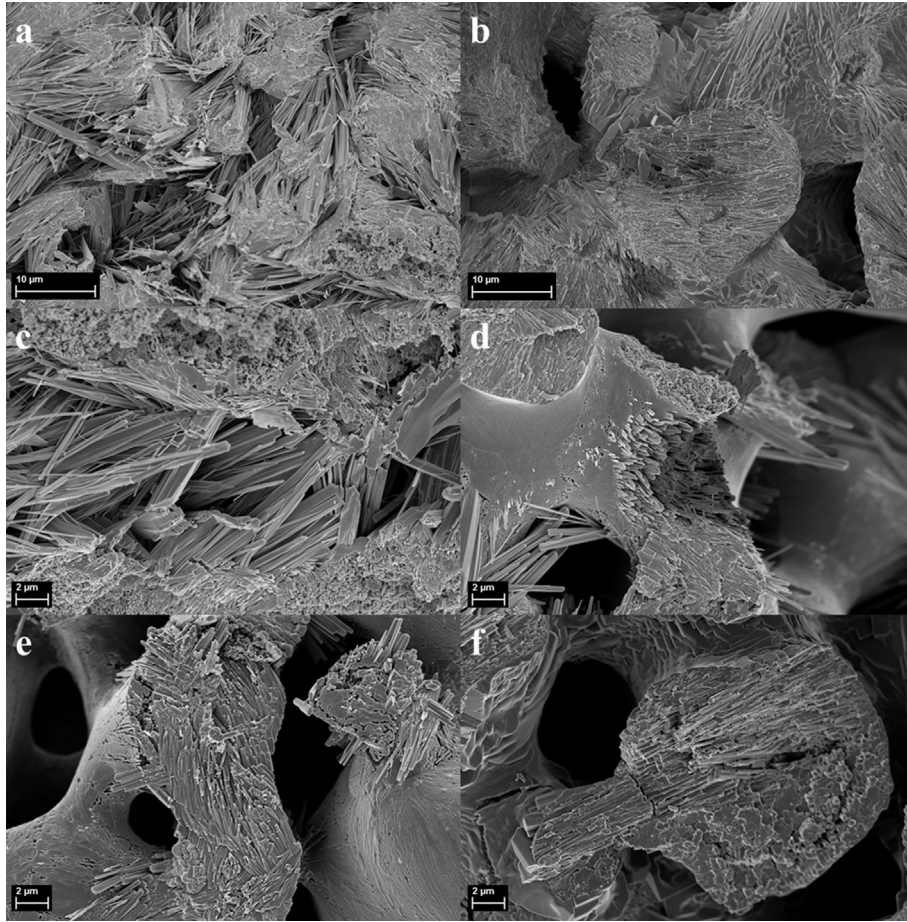


Fig. 2. Effect of incubation temperature on the microstructure, especially on the location of crystal growth: a) 125 °C overview, b) 200 °C overview, c) 125 °C, d) 150 °C, e) 175 °C, f) 200 °C. Scale bars are 10 μm long in a) and b) and 2 μm long in c) to f).

The incubation time significantly influenced the mechanical properties of the ceramic blocks (ANOVA: $p < 0.0001$). Upon hydrothermal incubation at 200 °C, the diametral strength and the fracture energy (WOF) increased with increasing incubation time

(Fig. 6a), up to about 3.5 and 5 times the initial value, respectively. The strength and fracture energy reached the same values once complete phase conversion was achieved, whatever the incubation temperature was (from 125 °C to 200 °C) (Fig. 6b).

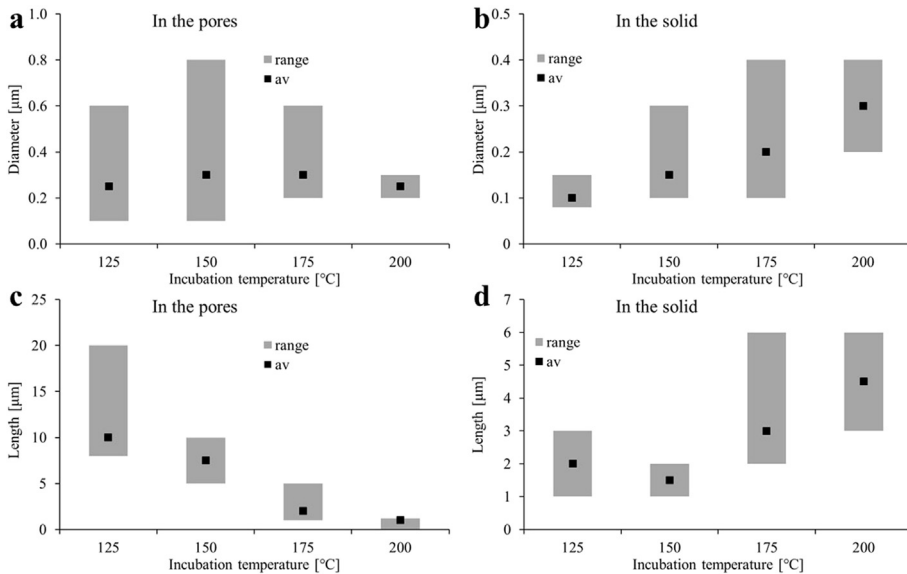


Fig. 3. a) and b) Diameter and c) and d) length of needle-like crystals in function of temperature and location: a) and c) in the initial porosity; b) and d) in the initial solid phase. The range (gray bar) covers the smallest to the largest measured values; the average value is represented by a black square.

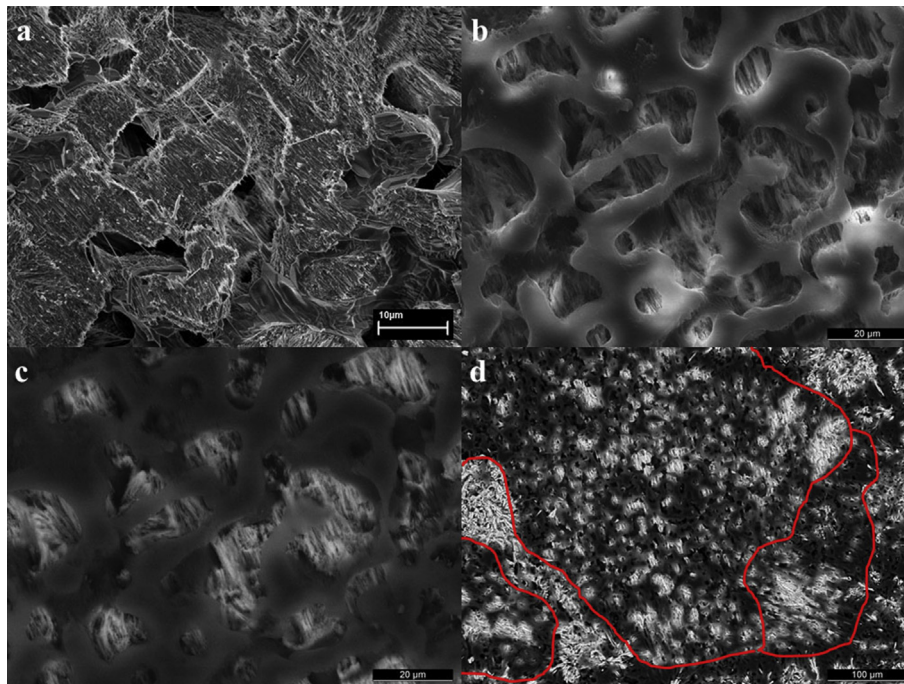


Fig. 4. a) The oriented domains were difficult to observe on broken or polished samples with SE because the magnification necessary to distinguish the crystals and their orientation was too high to observe the whole oriented areas (scale bar is 10 μm long). b) Embedding, polishing and chemically etching the samples better highlighted the needle crystals and their orientation, c) which was then better distinguished with BSE, d) and the extension of the oriented domains (red limits) was distinguishable at lower magnification. It was thus observed that oriented domains extending over hundreds of micrometers were also surrounded by smaller ones (scale bar is 100 μm long). (For interpretation of the references to colour in this figure legend, the reader is referred to the web version of this article.)

3.5. Fractured surfaces

The fractured surfaces after Brazilian tests were observed by SEM. The crack paths after sintering were flat and smooth throughout the samples. After hydrothermal treatment, the cracks in the dense solid parts were tortuous, as particularly observed with high incubation temperatures (Fig. 7). Indeed, crack deflection around needles and bundles of needles was well visible at 175 $^{\circ}\text{C}$ and at 200 $^{\circ}\text{C}$, when the crystal size increased.

4. Discussion

The aim of this study was to refine and create textured microstructures of CaP monoliths and obtain tortuous crack paths to increase their work of fracture, i.e. their toughness. Recrystallization in hydrothermal conditions was an effective way to texture the solid at the microscale without affecting macroscopic features like macroporosity (here, macropores are considered to have a size larger than 100 μm) and sample shape (Supplementary data, Figure S2 and Figure S3). Indeed, limiting direct contact with liquid water avoids extensive dissolution and reprecipitation which might provoke morphology changes at larger scale. Only with incubation at temperature lower than 150 $^{\circ}\text{C}$, crystals invaded the microporosity (Fig. 2a). At higher temperatures the microporosity was preserved (Fig. 2b). However, chemical and sub-micro structural changes occurred in all samples. Interestingly, when the structure was not densified by sintering prior to hydrothermal incubation, the newly formed needle-like CDHA crystals did not align [49,50] as confirmed by our own results of incubation of α -TCP powder-pressed samples (Supplementary data, Figure S4).

The strength improvement observed during the hydrothermal conversion of α -TCP into CDHA could be due to the higher intrinsic strength of HA compared to α -TCP (+120%) [51]. However, the

maximum mechanical improvements measured in this study were higher (+250%), implying that another mechanism is at play, for example better crystal entanglement or reduction of cracks. Beside an improvement of the tensile properties (Fig. 6), the recrystallization provoked by the hydrothermal treatment increased the work-of-fracture 5-fold. This might principally be due to the increase of strength without increase of stiffness, but a remarkable change of failure mode was also observed. Indeed, cracks propagated quite linearly through the smooth sintered structures, while the textured samples showed obvious crack deflection around densely packed and aligned crystals, but also around and through bundles of crystals (Fig. 7, Supplementary data Figure S5). In other words, the reduced grain or crystal size promoted a transition from a transgranular to an intergranular cracking mode [23] and the anisotropic crystal shape, combined with changing and random orientation of bundles further enhanced crack deflection.

The failure mode observed here is very similar to the “extrinsic toughening” mechanism [18] observed in natural ceramic-based composites. Indeed, the material itself is not toughened at the atomic or molecular scale, like an annealed metal, but the texture and hierarchical structure of the construct increases fracture resistance by obstructing crack propagation. Micro cracking, crack bridging and crack deflection are typical extrinsic toughening mechanisms occurring in densely packed crystalline phases [18] and can explain for instance the high fracture toughness observed in bone or nacre [52]. To obtain these effects in synthetic materials, a good control of microstructure is necessary. In glass ceramics, toughness values up to 2.7 $\text{MPa}\cdot\text{m}^{1/2}$ have been obtained [53,54], which is still in the lower range of cortical bone values (2–20 $\text{MPa}\cdot\text{m}^{1/2}$) [4,18,55,56], but higher than bioactive ceramics (0.5 $\text{MPa}\cdot\text{m}^{1/2}$).

The hydrothermal process led to two structural changes that may explain an increase of mechanical properties: a decrease of

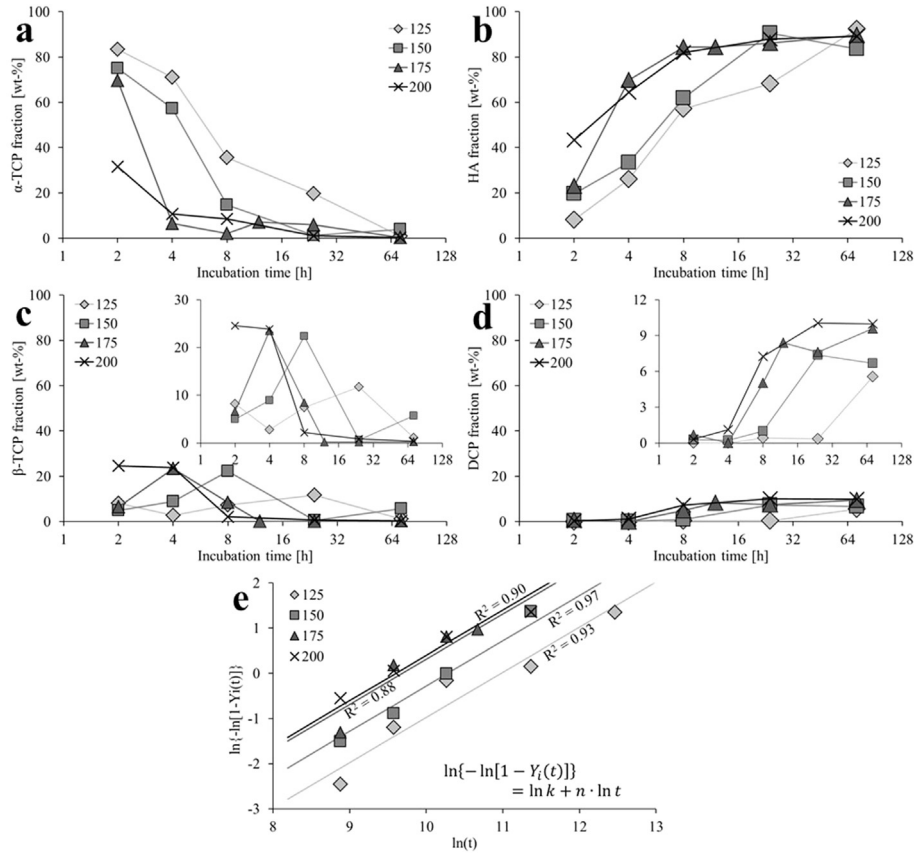


Fig. 5. Phase transformation (Rietveld refinement of XRD results) over incubation time at \blacklozenge 125 °C, \blacksquare 150 °C, \blacktriangle 175 °C, and \times 200 °C. a) consumption of initial α -TCP phase; b) formation of hydroxyapatite (HA); c) intermediate formation and consumption of β -TCP; d) formation of monetite (DCP); e) Avrami plot of the global phase transformation, with $Y_i(t) =$ combined consumption of α -TCP and β -TCP or combined formation of HA and DCP (with the slope $n = 1$).

Table 1

Parameters n and K for the Avrami fits of the phase conversions at different temperatures with the according correlation coefficients, R^2 . The activation energy E_a for each phase can then be obtained with the Arrhenius equation. The minus signs indicate disappearance of phases, whereas plus signs indicate formation. Color code: $0.7 < R^2$; $0.7 < R^2 < 0.8$; $0.8 < R^2 < 0.9$; $0.9 < R^2$.

	- α -TCP		+ β -TCP		- β -TCP		+ CDHA		+ DCP		- (α -TCP + β -TCP)		+ (CDHA + DCP)	
	n = 1		n = 1		n = 1		n = 1		n = 3		n = 1		n = 1	
	K	R^2	K	R^2	K	R^2	K	R^2	K	R^2	K	R^2	K	R^2
-ln(K_i)	10.66	0.95	13.14	0.84	10.78	0.77	10.84	0.94	36.69	0.98	10.97	0.93	10.97	0.93
125 °C	10.66	0.95	13.14	0.84	10.78	0.77	10.84	0.94	36.69	0.98	10.97	0.93	10.97	0.93
150 °C	9.96	0.96	11.82	0.96	9.80	0.99	10.11	0.95	32.57	0.99	10.28	0.97	10.28	0.97
175 °C	9.70	0.26	11.23	0.76	9.13	0.87	9.94	0.51	31.01	1.00	9.69	0.88	9.69	0.88
200 °C	9.50	0.87			8.90	0.65	9.52	0.79	31.00	0.81	9.60	0.90	9.60	0.90
E_a [kJ/mol]	24 \pm 4		57 \pm 11		40 \pm 6		26 \pm 4		119 \pm 37		30 \pm 5		30 \pm 5	

grain/crystal size and an increase in the number of hierarchical structures (Figs. 1, 2 and 4). The diametral tensile strength and the work of fracture were increased 4–5fold (Fig. 6a, c). However, since both parameters changed simultaneously, it is difficult to extract the single effect of the two factors. The fiber diameter and length increased 2–3fold when the incubation temperature was increased from 125 °C to 200 °C (Fig. 3b,d). As the mechanical properties and the failure mode were not affected by this change (Fig. 6b,d), this may suggest that the crystals were already small enough to change the mechanism of rupture from a transgranular to an intergranular

failure mode. To get more insight into the effect of architecture, the size and orientation of the oriented domains should be controlled. This is the topic of our current efforts.

The architecture of the present structures resembles those of natural composites like shells or teeth (Fig. 8). Even if the crystal phases and chemistry are different, elongated primary crystals are densely packed and aligned within domains in those three materials. Like in enamel of shark teeth [57], the obtained structures exhibit 5 levels of hierarchy: (i) hydroxyapatite crystalline structure, (ii) in the form of needle-like crystals, (iii) aligned in bundles,

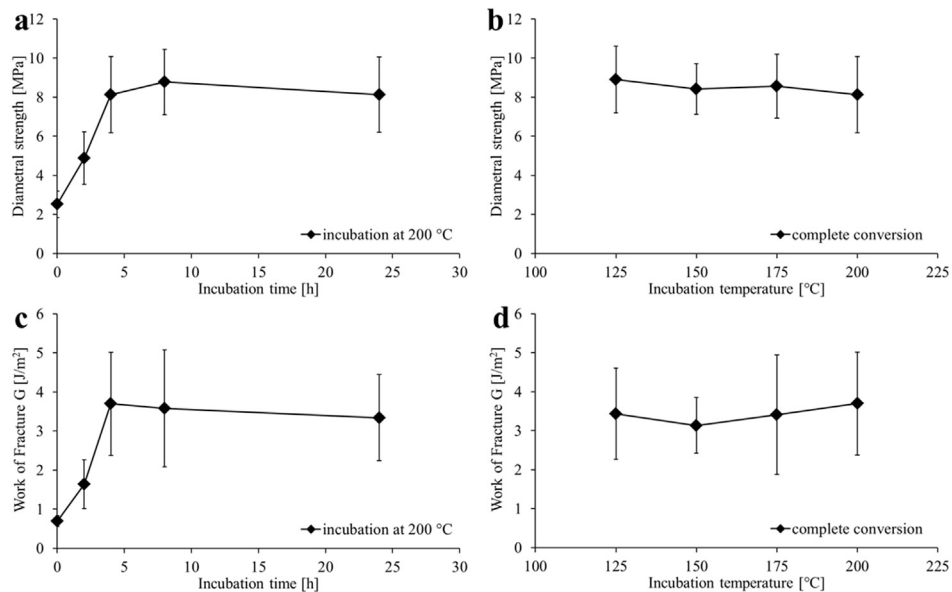


Fig. 6. a) and b) Diametral strength measured by Brazilian tests and c) and d) work-of-fracture calculated as the area under the stress–strain curve of the Brazilian tests. a) and c) As a function of the hydrothermal incubation time at 200 °C; b) and d) as a function of the hydrothermal incubation temperature for maximum conversion.

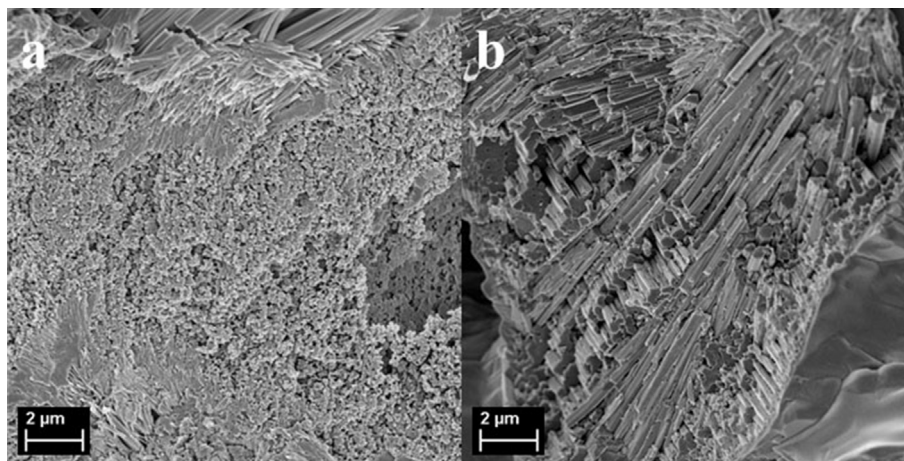


Fig. 7. Examples of fracture surfaces after Brazilian testing. With increasing temperature, the tortuosity (non-linearity) of the crack paths became increasingly visible as the crystal size increased: a) incubation at 125 °C; b) incubation at 200 °C.

(iv) which are stacked with random orientation to form (v) a macroscopic sample (Fig. 9). It has to be noticed that the crystals observed by Enax et al. [57] in enamel of shark teeth were about 5 times thinner (Fig. 8d and e) than the crystals observed in the present study (Fig. 8a), but crystals and domains sizes of shells were similar to those of the present samples (Fig. 8b and c). However, natural materials present large crystalline domains whose orientation is predefined and controlled, contrarily to the present materials where the domain orientation is uncontrolled. Also organic layers are intercalated between the crystalline domains in natural composites and bring some additional toughness (defined as “intrinsic toughening” in Refs. [18,21]). This might be introduced by impregnating the present porous and structured bioceramics with a tough polymer. Indeed, substantial improvements have been reported in the literature [58–61], for example a 7- to 13-fold increase of BCP toughness with PCL [62].

In the present study, it has been established that crystal texturing obtained by the conversion of α -TCP into CDHA leads to

extrinsic toughening: the degree of alignment and the size of domains of coherent crystal orientation obtained by hydrothermal conversion resulted in a substantial improvement of mechanical properties, which was, however, still far too limited to provide materials with load-bearing properties. On the other hand, the limit of orientation and coherent domain size was not reached. Larger mechanical improvements could thus most probably be obtained by further controlling the size and the orientation of the aligned domains. To reach this long-term goal, it appears important to understand how α -TCP converts to CDHA crystals and what parameters affect this conversion. The phase transformation of α -TCP to CDHA is therefore discussed thoroughly in the following sections.

Hydration in water vapor converted α -TCP mainly into CDHA (Fig. 5a and b), but two additional crystalline phases were also detected by XRD: β -TCP (Fig. 5c) as an intermediate phase and DCP (Fig. 5d). The presence of CDHA was expected because it is the normal end-product of the hydration reaction of α -TCP. Contrarily,

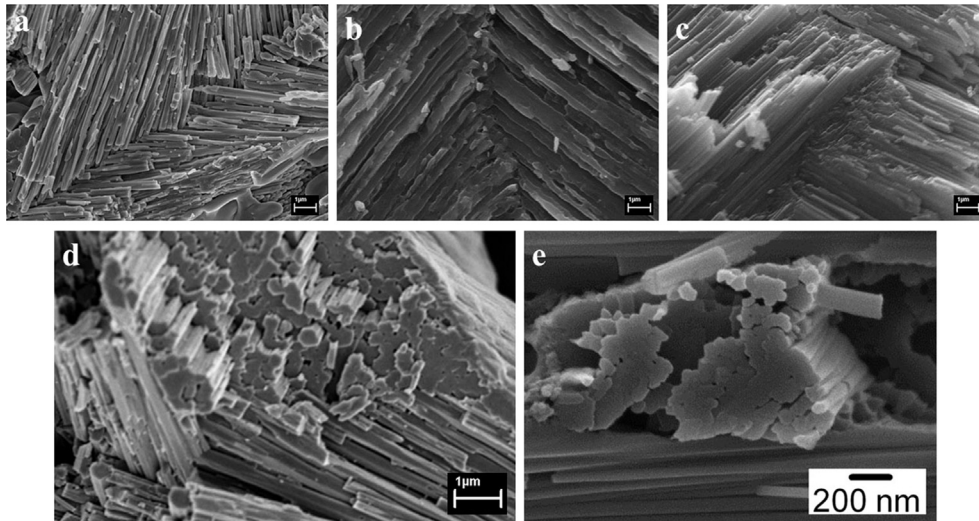


Fig. 8. Various SEM pictures to highlight the similarity of the microstructures obtained in the present study with natural materials. a) and d) Synthetic hydroxyapatite obtained by hydrothermal incubation for 24 h at 200 °C; b) *Acanthocardia aculeate*, Mediterranean shell; c) *Aporrhais pespelecani*, Mediterranean shell; e) Enamel of shark teeth [71]. Scale bars are 1 μm in a) to d), but 200 nm in e).

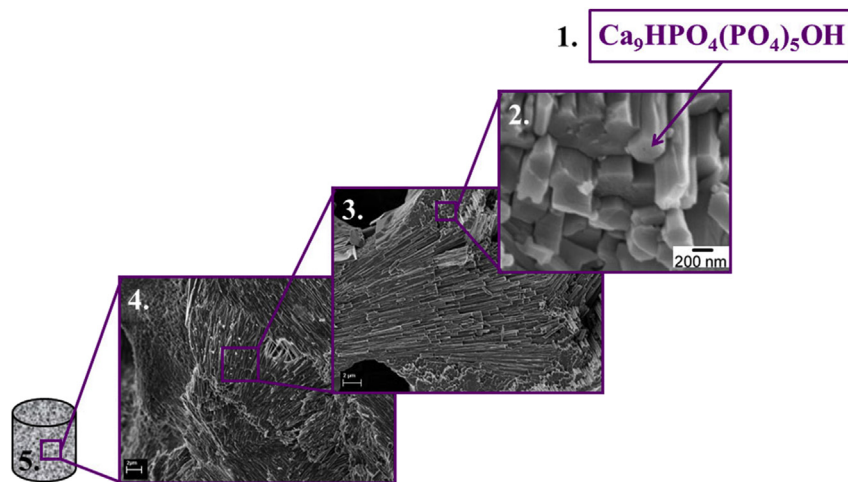
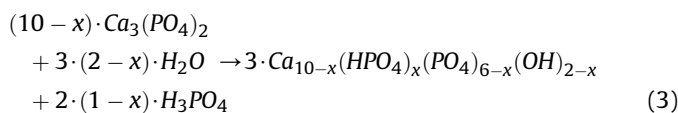


Fig. 9. Hierarchical structure: 1. CDHA crystalline structure 2. in the form of needles, 3. assembled in bundles, 4. stacked with random orientation, 5. to obtain a macroscopic ceramic block.

the formation of β -TCP was more surprising because β -TCP is generally obtained by solid state reaction above 700–800 °C [63]. However, a few recent studies have reported its precipitation in non-aqueous systems [64–66] and in hydrothermal conditions [67]. The second additional phase, namely DCP, appeared at the end of the reaction, after CDHA formation (Fig. 5b, d). This explains why the large prismatic crystals which have the typical morphology of DCP crystals [68] were seen at the solid surface (Fig. 1f). Since DCP is only more stable than CDHA at low pH [69], its appearance suggests an acidification of the reaction milieu over time, which was confirmed by pH-paper measurements indicating a value of about 4 in the solution. Chemically, acidification would occur if hydroxyapatite with a Ca/P molar ratio higher than 1.5 ($x < 1$) would form:



According to XRD data of calcined samples the overall Ca/P ratio

of the samples did not differ from 1.5 over time. The formation of DCP, which has a molar Ca/P ratio of 1.0, must thus be compensated by the formation of (CD)HA with a Ca/P ratio greater than 1.5 ($x < 1$). It is unclear whether the CDHA was depleted of its phosphate ions over time or whether a newly formed phase only consisting of HA with a Ca/P ratio greater than 1.5 was formed beside an initial CDHA with Ca/P = 1.5.

The XRD results may suggest that α -TCP first converted to β -TCP, which itself converted to CDHA and DCP. This phase stability order (α -TCP < β -TCP < CDHA, DCP) is the same as the one observed in slightly acidic conditions at room temperature [70,71]. Nevertheless, the formation of β -TCP as intermediate phase is intriguing. Indeed, it is known that the precipitation of hydrated phases such as brushite (dicalcium phosphate dihydrate, DCPD, $\text{CaHPO}_4 \cdot 2\text{H}_2\text{O}$) or octacalcium phosphate (OCP, $\text{Ca}_8\text{H}_2(\text{PO}_4)_6 \cdot 5\text{H}_2\text{O}$) are kinetically favored in aqueous conditions, and as a result precipitate before the most stable phases (DCP, HA) appear. Here, this scheme cannot be used because the most stable phase (CDHA) is also the hydrated phase. One alternative explanation could be that the pressure

applied on the system is able to drastically lower the equilibrium temperature between β -TCP and α -TCP, which is close to 1120 °C, and thus favor the allotropic transformation of α -TCP into β -TCP, β -TCP being 10% denser than α -TCP. The fact that β -TCP crystals could not be identified on the SEM images support the allotropic transformation mechanism. Despite the fact that it is assumed that α -TCP was first converted to β -TCP and then CDHA or DCP, it is also possible that part of the α -TCP was directly converted to CDHA or DCP.

The reaction of α -TCP blocks with water vapor not only led to chemical changes, but also to microstructural changes visible by SEM (Fig. 1). The obtained microstructures were different from those usually observed after hydration in physiological conditions (See supplementary data, Figure S4). Whereas the sintered α -TCP grains were a few micrometers large, the CDHA crystals were a few hundred of nanometers wide and up to a few micrometers long, aligned sometimes over hundreds of micrometers (Fig. 4). SEM images suggest that CDHA nucleation occurred on exposed surfaces (pores and cracks), followed by unidirectional progression into the solid. These nucleation and growth mechanisms were confirmed by the outcomes of the kinetic study (Fig. 5e and Table 1). Indeed, good fits of the experimental curves were obtained with Avrami's equation using a value of 1 for the n parameter, which indicate punctual nucleation and linear progression of phase conversion [72]. Using Avrami's equation, it was possible to calculate the activation energies for each phase conversion. The values obtained here for α -TCP and β -TCP conversion into DCP and CDHA (Fig. 5e) were only slightly larger than 20 kJ/mol, which is a typical value for reaction controlled reactions in aqueous solutions. From the reaction rate, it is possible to estimate a minimum value for the diffusion rate. The calculated value is close to 10^{-9} m²/s which is similar to diffusion of hydrogen in water at room temperature [73] and much higher than diffusion of atoms in solids. For example, it is about 10^4 times faster than hydrogen diffusion in α -Fe at 25 °C [73] or about 100 times faster than carbon diffusion in γ -Fe at 1000 °C [74]. In consequence the results suggest that diffusion actually occurred in a condensed water layer on the surface of the ceramic. The newly formed HA phase being denser (3.15 g/cc) than the initial α -TCP phase (2.87 g/cc), it creates space for further diffusion into the solid.

At low incubation temperature, CDHA needles grew both in the initially solid regions (struts), and in the micropores. The needle-like CDHA crystals were aligned and densely packed at the former location of the dense struts (Fig. 2). In the initial micropore regions, CDHA crystals were more loosely packed and less aligned (Fig. 2a and c). Increasing the incubation temperature affected the synthesized structures in two ways: first, recrystallization was more and more confined to the initially dense parts. Second, the crystal size in the initially dense parts (struts) increased with the incubation temperature (Fig. 3), which may be attributed to increased dissolution and diffusion rates.

5. Conclusions

CaP ceramics with highly aligned crystals were obtained by hydrothermal transformation of sintered α -TCP blocks into CDHA blocks. Complex architectures, with five hierarchical levels were reached in pure CaP ceramic scaffolds. This was achieved by recrystallization of sintered blocks *in situ*. The resulting crystals were much thinner than the initial sintered grains and had an elongated shape. The needles aligned over a distance depending mainly on incubation temperature, thus forming oriented domains. The higher the incubation temperature, the denser the crystals and aligned domains were packed. Also, crystals became longer and thicker.

One consequence of texturing CaP ceramics by hydrothermal treatment was a 5-fold increase of work-of-fracture. The results suggest that this increase was due to the so-called "extrinsic toughening" mechanism, i.e. mainly crack deflection, as observed in many natural materials. Interestingly, cracks were deflected at two levels: around needle-like crystals, but also around aligned domains, or bundles of crystals. Further improvement of mechanical properties would require a better control over needle size, aligned domain size and global domain orientation. Differences in vapor pressure and diffusion rates between solid and pores might explain packing differences at different temperatures; however the whole recrystallization process is still unclear. Additives acting as growth inhibitors or accelerators, like citrates, pyrophosphates or magnesium, while incubating at high temperature (200 °C) might lead to reduced but even more confined growth of CDHA crystals.

The toughness could be even more enhanced by incorporation of some organic phases by polymer impregnation, for example. In this case, hydrothermal incubation at low temperatures might be more adequate to preserve some porosity in between bundles, or even crystals to allow proper polymer penetration.

Overall, the processing route described in this work provides an effective pathway for the fabrication of highly textured calcium phosphate-based ceramics exhibiting unique microstructural features at multiple length scales.

Acknowledgments

The authors would like to thank Mathys Ltd, Bettlach (Switzerland) for their financial support.

Appendix A. Supplementary data

Supplementary data related to this article can be found at <http://dx.doi.org/10.1016/j.biomaterials.2015.07.026>.

References

- [1] R.Z. LeGeros, Properties of osteoconductive biomaterials: calcium phosphates, *Clin. Orthop.* (2002) 81–98.
- [2] P.V. Giannoudis, H. Dinopoulos, E. Tsiridis, Bone substitutes: an update, *Injury* 36 (Suppl. 3) (2005).
- [3] P.S. Eggli, W. Muller, R.K. Schenk, Porous hydroxyapatite and tricalcium phosphate cylinders with two different pore size ranges implanted in the cancellous bone of rabbits. A comparative histomorphometric and histologic study of bony ingrowth and implant substitution, *Clin. Orthop.* (1988) 127–138.
- [4] E. Munch, M.E. Launey, D.H. Alsem, E. Saiz, A.P. Tomsia, R.O. Ritchie, Tough, bio-inspired hybrid materials, *Science* 322 (2008) 1516–1520.
- [5] R.O. Ritchie, The conflicts between strength and toughness, *Nat. Mater* 10 (2011) 817–822.
- [6] F. Witte, The history of biodegradable magnesium implants: a review, *Acta Biomater.* 6 (2010) 1680–1692.
- [7] M. Peuster, C. Hesse, T. Schloo, C. Fink, P. Beerbaum, C. von Schnakenburg, Long-term biocompatibility of a corrodible peripheral iron stent in the porcine descending aorta, *Biomaterials* 27 (2006) 4955–4962.
- [8] M. Schinhammer, A.C. Hänzli, J.F. Löffler, P.J. Uggowitzer, Design strategy for biodegradable Fe-based alloys for medical applications, *Acta Biomater.* 6 (2010) 1705–1713.
- [9] A.A. Ignatius, O. Betz, P. Augat, L.E. Claes, In vivo investigations on composites made of resorbable ceramics and poly(lactide) used as bone graft substitutes, *J. Biomed. Mater. Res.* 58 (2001) 701–709.
- [10] W. Bonfield, M. Grynias, A.E. Tully, J. Bowman, J. Abram, Hydroxyapatite reinforced polyethylene—a mechanically compatible implant material for bone replacement, *Biomaterials* 2 (1981) 185–186.
- [11] Y. Shikunami, M. Okuno, Bioresorbable devices made of forged composites of hydroxyapatite (HA) particles and poly-L-lactide (PLLA): part I. Basic characteristics, *Biomaterials* 20 (1999) 859–877.
- [12] J. Venkatesan, S.K. Kim, Chitosan composites for bone tissue engineering – an overview, *Mar. Drugs* 8 (2010) 2252–2266.
- [13] A. Baji, S.C. Wong, T.S. Srivatsan, G.O. Njus, G. Mathur, Processing methodologies for polycaprolactone-hydroxyapatite composites: a review, *Mater. Manuf. Process* 21 (2006) 211–218.
- [14] S.S. Kim, M. Sun Park, O. Jeon, C. Yong Choi, B.S. Kim, Poly(lactide-co-

- glycolide)/hydroxyapatite composite scaffolds for bone tissue engineering, *Biomaterials* 27 (2006) 1399–1409.
- [15] Q. Hu, B. Li, M. Wang, J. Shen, Preparation and characterization of biodegradable chitosan/hydroxyapatite nanocomposite rods via in situ hybridization: a potential material as internal fixation of bone fracture, *Biomaterials* 25 (2004) 779–785.
- [16] K. Rezwani, Q.Z. Chen, J.J. Blaker, A.R. Boccaccini, Biodegradable and bioactive porous polymer/inorganic composite scaffolds for bone tissue engineering, *Biomaterials* 27 (2006) 3413–3431.
- [17] R.E. Neuendorf, E. Saiz, A.P. Tomsia, R.O. Ritchie, Adhesion between biodegradable polymers and hydroxyapatite: Relevance to synthetic bone-like materials and tissue engineering scaffolds, *Acta Biomater.* 4 (2008) 1288–1296.
- [18] Q. Fu, E. Saiz, M.N. Rahaman, A.P. Tomsia, Toward strong and tough glass and ceramic scaffolds for bone repair, *Adv. Funct. Mater.* 23 (2013) 5461–5476.
- [19] L.J. Bonderer, A.R. Studart, L.J. Gauckler, Bioinspired design and assembly of platelet reinforced polymer films, *Science* 319 (2008) 1069–1073.
- [20] M.E. Launey, E. Munch, D.H. Alsem, H.B. Barth, E. Saiz, A.P. Tomsia, et al., Designing highly toughened hybrid composites through nature-inspired hierarchical complexity, *Acta Mater.* 57 (2009) 2919–2932.
- [21] R.O. Ritchie, J.H. Kinney, J.J. Kruzic, R.K. Nalla, A fracture mechanics and mechanistic approach to the failure of cortical bone, *Fatigue Fract. Eng. Mater. Struct.* 28 (2005) 345–371.
- [22] Z. Shen, M. Johnsson, Z. Zhao, M. Nygren, Spark plasma sintering of alumina, *J. Am. Ceram. Soc.* 85 (2002) 1921–1927.
- [23] J. Wang, L.L. Shaw, Nanocrystalline hydroxyapatite with simultaneous enhancements in hardness and toughness, *Biomaterials* 30 (2009) 6565–6572.
- [24] R.H.J. Hannink, P.M. Kelly, B.C. Muddle, Transformation toughening in zirconia-containing ceramics, *J. Am. Ceram. Soc.* 83 (2000) 461–487.
- [25] R.M. McMeeking, A.G. Evans, Mechanics of Transformation-toughening in Brittle Materials, 5 ed, 1982, pp. 242–246.
- [26] M. Yoshimura, Phase stability of zirconia, *Am. Ceram. Soc. Bull.* 67 (1988) 1950–1955.
- [27] A. Masahiro, I. Eiichi, M. Taishi, H. Masahiro, Elastic modulus, strength and fracture toughness of alumina ceramics containing pores, *J. Ceram. Soc. Jpn.* 110 (2002) 554–559.
- [28] K.T. Faber, A.G. Evans, Crack deflection processes-I, Theory, *Acta Metall.* 31 (1983) 565–576.
- [29] G.D. Zhan, J.D. Kuntz, J. Wan, A.K. Mukherjee, Single-wall carbon nanotubes as attractive toughening agents in alumina-based nanocomposites, *Nat. Mater.* 2 (2003) 38–42.
- [30] F. Bouville, E. Maire, S. Meille, B. Van de Moortèle, A.J. Stevenson, S. Deville, Strong, tough and stiff bioinspired ceramics from brittle constituents, *Nat. Mater.* 13 (5) (2014) 508–514.
- [31] M. Mazaheri, M. Haghighatzadeh, A.M. Zahedi, S.K. Sadrnezhad, Effect of a novel sintering process on mechanical properties of hydroxyapatite ceramics, *J. Alloys Compd.* 471 (2009) 180–184.
- [32] H. Zhang, B.W. Darvell, Synthesis and characterization of hydroxyapatite whiskers by hydrothermal homogeneous precipitation using acetamide, *Acta Biomater.* 6 (2010) 3216–3222.
- [33] M. Yoshimura, H. Suda, K. Okamoto, K. Ioku, Hydrothermal synthesis of biocompatible whiskers, *J. Mater. Sci.* 29 (1994) 3399–3402.
- [34] H. Yamasaki, Heterotopic bone formation around porous hydroxyapatite ceramics in the subcutis of dogs, *Jpn. J. Oral Biol.* 32 (1990) 190–192.
- [35] S. Dasgupta, S. Tarafder, A. Bandyopadhyay, S. Bose, Effect of grain size on mechanical, surface and biological properties of microwave sintered hydroxyapatite, *Mater. Sci. Eng. C* 33 (2013) 2846–2854.
- [36] D. Lahiri, V. Singh, A.K. Keshri, S. Seal, A. Agarwal, Carbon nanotube toughened hydroxyapatite by spark plasma sintering: microstructural evolution and multiscale tribological properties, *Carbon* 48 (2010) 3103–3120.
- [37] G. Kawachi, H. Misumi, H. Fujimori, S. Goto, C. Ohtsuki, M. Kamitakahara, et al., Fabrication of porous blocks of calcium phosphate through hydrothermal processing under glycine coexistence, *J. Ceram. Soc. Jpn.* 118 (2010) 559–563.
- [38] K. Ioku, G. Kawachi, S. Sasaki, H. Fujimori, S. Goto, Hydrothermal preparation of tailored hydroxyapatite, *J. Mater. Sci.* 41 (2006) 1341–1344.
- [39] T. Okuda, K. Ioku, I. Yonezawa, H. Minagi, Y. Gonda, G. Kawachi, et al., The slow resorption with replacement by bone of a hydrothermally synthesized pure calcium-deficient hydroxyapatite, *Biomaterials* 29 (2008) 2719–2728.
- [40] C. Antoine, Tensions des vapeurs: nouvelle relation entre les tensions et les températures, *Comptes Rendus Séances l'Académie Sci.* 107 (1888), 681–4, 778–80, 836–7.
- [41] T. Taut, R. Kleeberg, J. Bergmann, The new Seifert Rietveld program BGMN and its application to quantitative phase analysis, *Mater. Struct.* 5 (1998) 57–66.
- [42] L.W. Schroeder, B. Dickens, W.E. Brown, Crystallographic studies of the role of Mg as a stabilizing impurity in b-Ca₃(PO₄)₂. II. Refinement of Mg-containing b-Ca₃(PO₄)₂, *J. Solid State Chem.* 22 (1977) 253–262.
- [43] M. Mathew, L.W. Schroeder, B. Dickens, W.E. Brown, The crystal structure of a-Ca₃(PO₄)₂, *Acta Cryst. B* 33 (1977) 1325–1333.
- [44] K. Sudarsanan, R.A. Young, Significant precision in crystal structure details: Holly springs hydroxyapatite, *Acta Cryst. B* 25 (1969) 1534–1543.
- [45] B. Dickens, J.S. Bowen, W.E. Brown, A refinement of the crystal structure of CaHPO₄ (synthetic monetite), *Acta Cryst. B* 28 (1971) 797–806.
- [46] P.O. Bouchard, F. Bay, Y. Chastel, I. Tovena, Crack propagation modelling using an advanced remeshing technique, *Comput. Methods Appl. Mech. Eng.* 189 (2000) 723–742.
- [47] K. Ishikawa, P. Ducheyne, S. Radin, Determination of the Ca/P Ratio in Calcium-Deficient Hydroxyapatite Using X-Ray-Diffraction Analysis, *J. Mater. Sci-Mater. M.* 4 (1993) 165–168.
- [48] M. Avrami, Kinetics of phase change. I: general theory, *J. Chem. Phys.* 7 (1939) 1103–1112.
- [49] H. Wakae, A. Takeuchi, K. Udoh, S. Matsuya, M.L. Munar, R.Z. LeGeros, et al., Fabrication of macroporous carbonate apatite foam by hydrothermal conversion of β -tricalcium phosphate in carbonate solutions, *J. Biomed. Mater. Res. - Part A* 87 (2008) 957–963.
- [50] S. Karashima, A. Takeuchi, S. Matsuya, K.I. Udoh, K. Koyano, K. Ishikawa, Fabrication of low-crystallinity hydroxyapatite foam based on the setting reaction of α -tricalcium phosphate foam, *J. Biomed. Mater. Res. - Part A* 88 (2009) 628–633.
- [51] L. Liang, P. Rulis, W.Y. Ching, Mechanical properties, electronic structure and bonding of α - and β -tricalcium phosphates with surface characterization, *Acta Biomater.* 6 (2010) 3763–3771.
- [52] M.E. Launey, M.J. Buehler, R.O. Ritchie, On the mechanistic origins of toughness in bone, *Annu. Rev. Mater. Res.* (2010) 25–53.
- [53] E. Apel, J. Deubener, A. Bernard, M. Höland, R. Müller, H. Kappert, et al., Phenomena and mechanisms of crack propagation in glass-ceramics, *J. Mech. Behav. Biomed. Mater.* 1 (2008) 313–325.
- [54] T. Kokubo, H.M. Kim, M. Kawashita, Novel bioactive materials with different mechanical properties, *Biomaterials* 24 (2003) 2161–2175.
- [55] J.D. Currey, P. Zioupos, P. Davies, A. Casinos, Mechanical properties of nacre and highly mineralized bone, *Proc. R. Soc. B Biol. Sci.* 268 (2001) 107–111.
- [56] B. Ji, H. Gao, Mechanical properties of nanostructure of biological materials, *J. Mech. Phys. Solids* 52 (2004) 1963–1990.
- [57] J. Enax, A.M. Janus, D. Raabe, M. Epple, H.O. Fabritius, Ultrastructural organization and micromechanical properties of shark tooth enameloid, *Acta Biomater.* 10 (9) (2014) 3959–3968.
- [58] Q.Z. Chen, A.R. Boccaccini, Poly(D,L-lactic acid) coated 45S5 Bioglass®-based scaffolds: Processing and characterization, *J. Biomed. Mater. Res. - Part A* 77 (2006) 445–457.
- [59] T. Mantsos, X. Chatzistavrou, J.A. Roether, L. Hupa, H. Arstila, A.R. Boccaccini, Non-crystalline composite tissue engineering scaffolds using boron-containing bioactive glass and poly(D,L-lactic acid) coatings, *Biomed. Mater. (Bristol)* 4 (2009).
- [60] V. Mourino, P. Newby, A.R. Boccaccini, Preparation and characterization of gallium releasing 3-d alginate coated 45s5 bioglass® based scaffolds for bone tissue engineering, *Adv. Eng. Mater.* 12 (2010). B283–B291.
- [61] Q. Fu, E. Saiz, M.N. Rahaman, A.P. Tomsia, Bioactive glass scaffolds for bone tissue engineering: State of the art and future perspectives, *Mater. Sci. Eng. C* 31 (2011) 1245–1256.
- [62] M. Peroglio, L. Gremillard, J. Chevalier, L. Chazeau, C. Gauthier, T. Hamaide, Toughening of bio-ceramics scaffolds by polymer coating, *J. Eur. Ceram. Soc.* 27 (2007) 2679–2685.
- [63] S.V. Dorozhkin, M. Epple, Biological and medical significance of calcium phosphates, *Angew. Chem. Int. Ed. Engl.* 41 (2002) 3130–3146.
- [64] J.S. Bow, S.C. Liou, S.Y. Chen, Structural characterization of room-temperature synthesized nano-sized beta-tricalcium phosphate, *Biomaterials* 25 (2004) 3155–3161.
- [65] J. Tao, W. Jiang, H. Zhai, H. Pan, R. Xu, R. Tang, Structural components and anisotropic dissolution behaviors in one hexagonal single crystal of b-tricalcium phosphate, *Cryst. Growth Des.* 8 (2008) 2227–2234.
- [66] L. Galea, M. Bohner, J. Thuerling, N. Doebelin, C.G. Aneziris, T. Graule, Control of the size, shape and composition of highly uniform, non-agglomerated, sub-micrometer β -tricalcium phosphate and dicalcium phosphate platelets, *Biomaterials* 34 (2013) 6388–6401.
- [67] T. Toyama, K. Nakashima, T. Yasue, Hydrothermal synthesis of β -tricalcium phosphate from amorphous calcium phosphate, *J. Ceram. Soc. Jpn.* 110 (2002) 716–721.
- [68] L.G. Galea, M. Bohner, J. Lemaitre, T. Kohler, R. Muller, Bone substitute: Transforming b-tricalcium phosphate porous scaffolds into monetite, *Biomaterials* 29 (2008) 3400–3407.
- [69] G. Vereecke, J. Lemaitre, Calculation of the solubility diagrams in the system Ca(OH)₂-H₃PO₄-KOH-HNO₃-CO₂-H₂O, *J. Cryst. Growth* 104 (1990) 820–832.
- [70] F.C.M. Driessens, R.M. Verbeeck, Relation between physico-chemical solubility and biodegradability of calcium phosphates, in: C. de Putter, G.L. de Lange, K. De Groot, A.J.C. Lee (Eds.), *Advances in Biomaterials*, Elsevier Science Publishers, Amsterdam, 1988, pp. 105–111.
- [71] M. Bohner, *Bioresorbable ceramics*, in: F. Buchanan (Ed.), *Degradation Rate of Bioresorbable Materials*, Woodhead Publishing Limited, Cambridge, 2008, pp. 95–114.
- [72] A. Karamanov, I. Avramov, L. Arrizza, R. Pascova, I. Gutzow, Variation of Avrami parameter during non-isothermal surface crystallization of glass powders with different sizes, *J. Non Cryst. Solids* 358 (2012) 1486–1490.
- [73] E.L. Cussler, *Diffusion - Mass Transfer in Fluid Systems*, Cambridge University Press, Cambridge, United Kingdom, 1984.
- [74] D.A. Porter, K.E. Easterling, *Phase Transformations in Metals and Alloys*, Van Nostrand Reinhold (UK) Co. Ltd, Molly Millars Lane, Wokingham, Berkshire, England, 1981.